Dalton Transactions

ROYAL SOCIETY OF CHEMISTRY

PAPER

View Article Online
View Journal | View Issue

Cite this: *Dalton Trans.*, 2024, **53**, 19272

Synthesis, characterization and chemical bonding analysis of the quaternary cyanamides $Li_2MnHf_2(NCN)_6$ and $Li_2MnZr_2(NCN)_6$†

Hicham Bourakhouadar, Juan Medina-Jurado, Peter C. Müller, Alex J. Corkett * and Richard Dronskowski *

$Li_2MnHf_2(NCN)_6$ and $Li_2MnZr_2(NCN)_6$ were prepared *via* solid-state metathesis reactions either *via* a more exothermic direct reaction between Li_2NCN, $MnCl_2$ and $HfCl_4$ or a milder two-step reaction in which ternary $Li_2Zr(NCN)_3$ was first prepared and subsequently reacted with MnF_2. Their crystal structures were determined from powder X-ray diffraction data and found to crystallize isotypically in low-symmetry variants of the [NiAs]-type MNCN structure with $P\bar{3}1m$ symmetry and comprise corundum-like $[T_2(NCN)_3]^{2+}$ layers (T = Hf^{4+}, Zr^{4+}) alternating with $[Li_2Mn(NCN)_3]^{2-}$ layers. In-depth chemical bonding analysis was undertaken using LOBSTER to calculate the Löwdin charges which reveal significant differences in covalency between the two metal layers that is also reflected in the crystal orbital bond indices (COBI) of the metal–nitrogen bonds as well as the carbon–nitrogen bonds that show distinct single and triple bond character, which is also evident from infrared spectroscopy measurements. A geometric analysis of all known quaternary cyanamides with the general formula $A_2MT_2(NCN)_6$ (A: an alkali metal, M: a divalent metal and T: a tetravalent metal) demonstrates the adaptation of the NCN unit to cation size differences, expressed as total distortion δ_{total}, by tilting away from the stacking axis. This tilting impacts the octahedral environment of the three different metal sites causing a distortion, quantified by means of the quadratic elongation λ_{oct}, revealing that the divalent and alkali metal sites are strongly dependent on δ_{total} whilst the tetravalent site is less influenced by the total distortion. Electronic structure calculations reveal $Li_2MnHf_2(NCN)_6$ to have an indirect band gap with a wide band gap of approximately 2.4 eV, in good agreement with the measured value of 2.1 eV. Furthermore, SQUID magnetometry measurements reveal predominantly antiferromagnetic interactions, but no transition to a long-range ordered state, presumably as a result of the magnetic dilution of the octahedral site, in which only 1/6 of the interstices are occupied by paramagnetic cations.

Received 12th September 2024,
Accepted 16th October 2024

DOI: 10.1039/d4dt02615b

rsc.li/dalton

Introduction

Research into NCN-containing compounds has received particular and increasing attention in recent years.[1] From a HSAB "hard and soft (Lewis) acids and bases" perspective, the NCN^{2-} anion lies between oxide O^{2-} and sulfide S^{2-}, thus prompting it to be considered as a pseudochalcogenide or "divalent nitride". Being also metastable and more covalent than their oxide analogues, carbodiimides often exhibit divergent properties and therefore hold great potential for a whole range of practical applications. Specifically, metal carbodiimides have been exploited as negative electrode materials in Na- or Li-ion batteries,[2,3] and also in photovoltaic devices,[4] fluorescent light sources[5,6] and light-emitting diodes.[7,8] From a structural point of view, many of these compounds can be derived from their oxide-analogues by replacing O^{2-} with the extended NCN^{2-} anion, either in its symmetric carbodiimide ($^{-}N{=}C{=}N^{-}$) or asymmetric cyanamide form ($N{\equiv}C{-}N^{2-}$), with structures generally consisting of layers of the NCN unit in either a hexagonal closed arrangement, derived from NiAs, or in a cubic closed arrangement, derived from NaCl. The metals in turn occupy the octahedral holes, so that an alternating anion-metal layered arrangement is obtained.

Unlike their respective oxide analogues, metal carbodiimides and cyanamides are generally not prepared by the conventional ceramic method due to their often endothermic nature. Synthesis of these compounds requires milder con-

Chair of Solid-State and Quantum Chemistry, Institute of Inorganic Chemistry, RWTH Aachen University, 52056 Aachen, Germany.
E-mail: drons@HAL9000.ac.rwth-aachen.de, alexander.corkett@ac.rwth-aachen.de

†Electronic supplementary information (ESI) available. CCDC 2382982 and 2382983. For ESI and crystallographic data in CIF or other electronic format see DOI: https://doi.org/10.1039/d4dt02615b

ditions, such as those offered by solid-state metathesis (SSM) reactions,[9] which have proven particularly effective. Such reactions are highly exothermic and promoted by the release of the lattice energy of the co-produced metathesis salt. Indeed, the application of the SSM reaction has given rise to a wide variety of binary, ternary, quaternary metal carbodiimides/cyanamides. The simplest examples of this group of compounds are binary representatives (*M*NCN) which adopt either a rhombohedral structure that derives from NaCl (this is the case for MnNCN, MgNCN, CaNCN, CdNCN, SrNCN) or a hexagonal structure,[10–13] which relates to NiAs (for FeNCN, CoNCN, NiNCN).[14,15] The ternary family of compounds $AM^{III}(NCN)_2$ (A = Li or Na, M = Al, In, Yb, Y, Sc) adopt a low-symmetry orthorhombic modification of NiAs, with a zigzag arrangement of the two metal channels,[16–18] and there are also perovskite-like phases of the $M^{II}Hf^{IV}(NCN)_3$ (M = Mn, Fe) type.[19] Common to all these compounds is the fact that they can all be described by a close relation to their oxide or chalcogenide analogues. However, the NCN unit distinguishes itself with its ability to tilt away from the stacking axis in order to accommodate metals of different sizes into the cationic layers, in a distortion that is not accessible to the spherical oxygen anion. In this way, the sizes of ions incorporated in the structures of metal carbodiimides/cyanamides play an important role in the stability of the structures, and can even allow for vacancies in the layers, as is seen in $Hf(NCN)_2$ and $Zr(NCN)_2$ which adopt vacancy-ordered NiAs derived structures with an open 'wine-rack' like framework.[20]

These observations highlighting a similarity to binary metal oxides and chalcogenides are less apparent when it comes to the quaternary family $A_2M^{II}Sn_2^{IV}(NCN)_6$ (A = Li or Na, M = Mn, Fe, Co, Ni and Mg),[21–23] where vacancy and cation ordering schemes are combined, giving rise to structures unique to carbodiimide chemistry. The crystal structures of these compounds comprise layers of metal cations alternating with NCN^{2-} ions, with an intra- and inter-layer cation ordering schemes. Motivated by this work, and with the intention of expanding this family, the new quaternary cyanamides $Li_2MnHf_2(NCN)_6$ and $Li_2MnZr_2(NCN)_6$ have been prepared. In addition, characterization by powder X-ray diffraction, infrared spectroscopy and chemical bonding analysis by means of DFT calculations are presented together with a detailed analysis of how the replacement of Sn^{4+} ions by Hf^{4+} or Zr^{4+} ions affect the coordination environments of the metals.

Experimental

Synthesis of $Li_2MnHf_2(NCN)_6$

In an argon filled glovebox a 6 : 1 : 2 stoichiometric ratio of Li_2NCN (prepared as described in ref. 24), $MnCl_2$ (ThermoFisher, 99.9%) and $HfCl_4$ (ThermoFisher, 98%, sublimed under dynamic vacuum at 200 °C for further purification) was homogenized, on the 0.4 g scale, in an agate pestle and mortar and loaded into a silica tube and sealed under vacuum. The sample was heated in a tubular furnace up to 700 °C and held at this temperature for 8 hours with heating and cooling rates of 2 °C min^{-1}. The accrued grayish colored sample (main yield 95%) proved stable to air. The product was washed with water and ethanol, before being dried at 100 °C.

Synthesis of $Li_2MnZr_2(NCN)_6$

A reaction mixture of the ternary compound $Li_2Zr(NCN)_3$ (prepared as described in ref. 25) and MnF_2 (ThermoFisher, 99%) was homogenized in an agate pestle and mortar, then loaded into a silica tube and sealed. The mixture was heated to 550 °C and the sample remained at this temperature for 8 hours with heating and cooling rates of 2 °C min^{-1}. The brown quaternary compound (main yield 92%) proved stable to air. The product was washed with water and ethanol, before being dried at 100 °C.

PXRD analysis

Powder X-ray diffraction (PXRD) data were recorded on a washed $Li_2MnHf_2(NCN)_6$ sample at room temperature using a calibrated STOE STADI-MP powder diffractometer with a flat sample holder (Mo $K_{\alpha1}$, linear PSD, 2θ range 3–65° with individual steps of 0.005°) and on washed $Li_2MnZr_2(NCN)_6$ using a calibrated STOE STADI-P powder diffractometer with a flat sample holder (Cu $K_{\alpha1}$, linear PSD, 2θ range 3–65° with individual steps of 0.005°). Rietveld refinements were performed using GSAS with the EXPGUI interface.[26] Full details concerning the structure determination including all intensity data are available in CIF format and have been deposited under the CCDC entry numbers 2382982 for $Li_2MnHf_2(NCN)_6$ and 2382983 for $Li_2MnZr_2(NCN)_6$.†

Infrared measurements

The infrared spectra of both quaternary cyanamides were measured on a Shimadzu IRSpirit FT-IR spectrometer.

CHN measurements

The chemical compositions of $Li_2MnHf_2(NCN)_6$ and $Li_2MnZr_2(NCN)_6$ were determined by CHN analysis using a Heraeus CHN-O Rapid analyser.

UV-Vis measurements

UV–Vis spectra of $Li_2MnHf_2(NCN)_6$ were recorded on a Shimadzu UV-2006 spectrophotometer. Tauc plots were calculated *via* the Kubelka–Munk function $F(R) = (1 - R)^2/2R$ to determine the bandgap size.

Computational details

The experimental structure of $Li_2MnHf_2(NCN)_6$ was optimized using Blöchl's projector augmented wave method[27] as implemented in the Vienna *ab initio* simulation package (VASP).[28–31] The exchange–correlation energy was modeled with the GGA-type functional PBEsol,[32] and an additional D3 term with Becke–Johnson damping[33] was employed to correct for dispersive interactions. The k-point meshes with a 11 × 11 × 7 point density was generated using the Monkhorst–Pack[34] scheme and integrated using Blöchl's tetrahedron method.[35] The kinetic-energy cutoff was chosen as 500 eV and conver-

gence criteria were set to 5×10^{-3} eV Å^{-1} (10^{-6} eV) for the ionic (electronic) iterations. Onsite correlation were corrected with a Hubbard *U*-parameter[36] of 3.90 eV, close to the self-consistent value used earlier (4.33 eV) for modelling the binary MnNCN.[37] For an accurate description of the electronic ground state of manganese, spin-polarization was enabled that resulted in a d^5 high-spin configuration of Mn.

After the structural optimization, a single point calculation was performed with the same setup as described above. The wave function generated thereby was unitarily transformed (projected) onto a local-orbital basis set using the LOBSTER program.[38–40] This atomic-orbital basis set enables the calculation of Löwdin charges[41] and bond orders by means of the crystal orbital bond index (COBI)[42] that is a generalization of the molecular Wiberg/Mayer bond index for periodic materials.[43–45] For deeper insight, an additional band-structure calculation was performed using Gaussian smearing for *k*-space integration due to technical reasons. All other parameters were kept constant.

SQUID-magnetometry

The magnetic properties were analysed with a Quantum Design (MPMS-5S, Quantum Design, San Diego) SQUID magnetometer. 10 mg of $Li_2MnHf_2(NCN)_6$ were placed in PTFE containers. Experimental data were collected in the temperature range between 2 K and 400 K at H = 1000 Oe. All data were corrected for diamagnetic contributions of the sample holder and the intrinsic contribution of the compound ($\chi_{m,dia}$ = –2.85 × 10^{-4} cm^3 mol^{-1}).

Results and discussion

The first quaternary transition metal cyanamide, namely $Li_2MnSn_2(NCN)_6$ was discovered in a quite unexpected way, since initial synthetic efforts were focused on the synthesis of ternary $MnSn(NCN)_3$.[21] However, the serendipitous incorporation of lithium from the precursor Li_2NCN resulted in the successful formation of $Li_2MnSn_2(NCN)_6$. With the aim of varying the tetravalent cation from Sn^{4+} to Hf^{4+} or Zr^{4+}, the quaternary $Li_2MnHf_2(NCN)_6$ was targeted *via* a solid-state metathesis reaction between Li_2NCN as a carbodiimide source, $MnCl_2$ and $HfCl_4$ at 700 °C as given in eqn. (1).

$$6\,Li_2NCN + MnCl_2 + 2\,HfCl_4 \rightarrow Li_2MnHf_2(NCN)_6 + 10\,LiCl \quad (1)$$

Attempts to synthesize the zirconium-containing analog *via* an equivalent direct 'three-component' reaction of Li_2NCN with the corresponding chlorides proved possible at 650 °C, leading to the desired quaternary, $Li_2MnZr_2(NCN)_6$, along with an as yet unknown by-product and a particularly large quantity of zirconium oxide. Therefore, an alternative, milder two-step reaction, which proved effective for the preparation of sodium-containing quaternaries $Na_2MSn_2(NCN)_6$ phases, was used.[22] Here the ternary metal carbodiimide was first prepared (eqn. (2))[25] and then reacted with the transition metal halide (eqn. (3)).

$$3\,Li_2NCN + ZrCl_4 \rightarrow Li_2Zr(NCN)_3 + 4\,LiCl \quad (2)$$

$$2\,Li_2Zr(NCN)_3 + MnF_2 \rightarrow Li_2MnZr_2(NCN)_6 + 2\,LiF \quad (3)$$

The observed powder X-ray reflections of $Li_2MnHf_2(NCN)_6$ were indexed to a hexagonal unit cell with lattice parameters a = 5.90691 Å, c = 9.6076 Å. A starting model of $Li_2MnHf_2(NCN)_6$ was generated from that of $Li_2MnSn_2(NCN)_6$ ($P\bar{3}1m$) by replacing Sn^{4+} with Hf^{4+} at the 2*c* position.[21] The tetravalent cation Zr^{4+} (0.72 Å, sixfold coordination)[46] has an almost equivalent size to that of Hf^{4+} (0.71 Å, sixfold coordination)[46] making hafnium easily replaced by zirconium at the 2*c* positions to obtain $Li_2MnZr_2(NCN)_6$ which crystallizes isotypically with lattice parameters a = 5.9479 Å, c = 9.6403 Å. The chemical formula of both quaternaries was verified by CHN analysis, which shows good agreement between experimental and calculated C and N contents (Table S1†). Rietveld refinements were then performed for both $Li_2MnHf_2(NCN)_6$ and $Li_2MnZr_2(NCN)_6$ phases starting from fully ordered $P\bar{3}1m$ models which resulted in good agreements to the observed data. However, further refinements permitting partial disorder between Li and Hf/Zr positions, whilst constraining both sites to be fully occupied, resulted in improved fits to the observed data and cation site disorder of 3.0(1) % and 5.6(1)% for the Hf and Zr analogues, respectively. In the final refinements, the results of which are summarized in Tables 1, 2 and S2,† the thermal displacement parameters (U_{iso}) of Li and Hf/Zr were constrained to be equal as were the U_{iso}s for all non-metal atoms (C and N) (Fig. 1).

The crystal structure of both new quaternary cyanamides derive from NiAs and relate to the aristotypic FeNCN by a group–subgroup relation.[14,48] Starting from FeNCN with $P6_3/mmc$ symmetry, through a *translationengleiche* transition (*t*2) the Fe site splits into two metal positions. A subsequent *klassengleiche* (*k*3) operation leads to a cell expansion and symmetry lowering from $P\bar{3}m1$ to $P\bar{3}1m$ resulting in four new metal positions (1*a*, 1*b*, 2*c*, 2*d*). The metal atoms arrange in two different layers, with both inter- and intra-layer cation ordering, one of fully occupied $[Li_2Mn(NCN)_3]^{2-}$ sheets and the

Table 1 Crystallographic data and fractional coordinates for $Li_2MnHf_2(NCN)_6$. Standard deviations are given in parentheses

Atom	Wyckoff site	x	y	z	*occ.*	U_{iso} (10^2 Å^2)
Li1	2*d*	$\frac{1}{3}$	$\frac{2}{3}$	$\frac{1}{2}$	0.970(1)	0.574(7)
Hf2	2*d*	$\frac{1}{3}$	$\frac{2}{3}$	$\frac{1}{2}$	1 – *occ.*(Li1)	"
Mn	1*b*	0	0	$\frac{1}{2}$	1	0.460(7)
Hf1	2*c*	$\frac{1}{3}$	$\frac{2}{3}$	0	*occ.*(Li1)	U_{iso}(Li1)
Li2	2*c*	$\frac{1}{3}$	$\frac{2}{3}$	0	1 – *occ.*(Li1)	U_{iso}(Li1)
N1	6*k*	0.689(1)	0	0.3834(6)	1	1.5(1)
N2	6*k*	0.590(1)	0	0.1298(6)	1	"
C	6*k*	0.642(2)	0	0.2672(7)	1	"

Trigonal, $P\bar{3}1m$ (No. 162), Z = 1, a = 5.90691(6) Å, c = 9.6076(2) Å; R_{wp} = 3.69%, R_p = 2.83%, χ^2 = 3.649, R_{wpb} = 4.25%.

Table 2 Selected bond lengths and angles in $Li_2MnHf_2(NCN)_6$ and $Li_2MnZr_2(NCN)_6$

$Li_2MnT_2(NCN)_6$	T = Hf	T = Zr
a (Å)	5.90691(6)	5.94790(12)
c (Å)	9.6076(2)	9.6403(3)
V (Å^3)	290.313(7)	295.358(13)
Bond lengths (Å)		
Li–N1 [6×]	2.326(4)	2.303(5)
Mn–N1 [6×]	2.151(6)	2.212(8)
T–N2 [6×]	2.179(4)	2.206(5)
C–N1	1.151(9)	1.202(13)
C–N2	1.355(9)	1.295(13)
Bond angles (°)		
N1–Li–N1	90.49(18), 77.0(2), 159.3(3), 105.8(3)	98.7(2), 83.6(3), 177.0(4), 98.7(2)
N2–T–N2	98.75(17), 77.02(3), 174.3(3), 85.7(2)	90.4(2), 77.8(3), 160.6(4), 104.9(5)
N1–C–N2	179.1(9)	174.9(15)

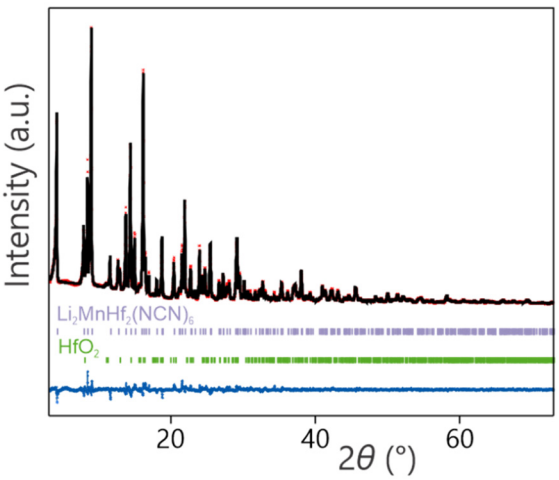

Fig. 1 Rietveld fit of $Li_2MnHf_2(NCN)_6$ to PXRD data, showing observed (red), calculated (black) and difference (blue) intensities. Bragg positions of $Li_2MnHf_2(NCN)_6$ (purple) and 7.80(7) wt.% HfO_2 baddeleyite $P2_1/c$ (green) are denoted by vertical markers.[47]

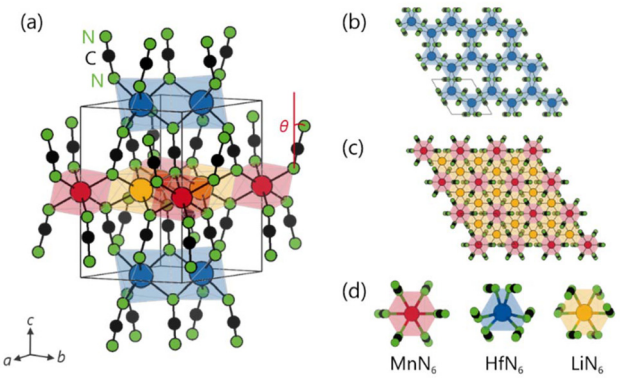

Fig. 2 Crystal structure of $Li_2MnHf_2(NCN)_6$ (a), view along the c direction of the vacancy-ordered $[Hf_2(NCN)_3]^{2+}$ layer (b), the $[Li_2Mn(NCN)_3]^{2-}$ layer (c) and metal-N_6 octahedra (d).

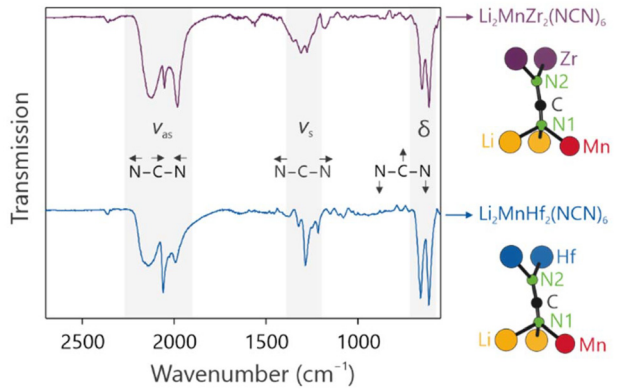

Fig. 3 Infrared spectra of $Li_2MnZr_2(NCN)_6$ (top left) and $Li_2MnHf_2(NCN)_6$ (bottom left). Coordination environment of the NCN unit in both quaternary structures (right).

other of only partially filled $[T_2(NCN)_3]^{2+}$ sheets with T as either Zr or Hf. These metal layers are linked by a hexagonal closed packing of cyanamide anions (Fig. 2).

The TN_6 octahedra with (T = Hf, Zr) have T–N bond lengths of 2.179(4) Å and 2.206(5) Å for hafnium and zirconium respectively, similar to the average distances in $Li_2T(NCN)_3$ (2.16 Å) (T = Hf, Zr) and therefore consistent with the presence of either a tetravalent hafnium or zirconium.[25] The LiN_6 (2.326(4) and 2.303(5) Å) and MnN_6 (2.151(6) and 2.212(8) Å) octahedra in both compounds are also similar to those seen in $Li_2MnSn_2(NCN)_6$ and indicative of Mn^{2+} and Li^+.[21]

A single crystallographically distinct NCN moiety is present in $Li_2MnHf_2(NCN)_6$ (Fig. 3, right), which is slightly bent with a bond angle of N1–C–N2 = 179.1(9)° and a tilting angle of θ = 13.5(3)°. However, two different C–N bond lengths are observed (C–N1 = 1.151(9) Å and C–N2 = 1.355(9) Å), which clearly evidence strong triple and single bond character as seen in $Li_2MnSn_2(NCN)_6$.[21] This is a result of the highly asymmetric coordination environment of the NCN moiety, which coordinates to two Hf^{4+} or Zr^{4+} cations at one end and to one Mn^{2+} cation and two Li^+ cations at the other, reducing the symmetry of the NCN anion shape to give a clear cyanamide character. This result is corroborated by IR measurements which show deformation vibrations (δ) between 600 and 700 cm^{-1}, asymmetric vibrations (ν_{as}) around 2100 cm^{-1} and a symmetric vibration (ν_s) around 1250 cm^{-1} that is IR forbidden for symmetric carbodiimide forms.

To better understand the chemical bonding in quaternary cyanamides, crystal orbital bond indices (COBI) as well as wave function-based Löwdin charges were calculated using LOBSTER for $Li_2MnHf_2(NCN)_6$.[40,42] The integrated COBI (=ICOBI) characterizes the covalent bond in the solid state by referring directly to the classical bond order. Löwdin charges as well as ICOBIs of all respective atoms are shown in Fig. 4.[41]

The oxidation states of Li^+, Mn^{2+} and Hf^{4+} correlate with Löwdin charges of +0.69e for Li, +1.31e for Mn and +1.51e for Hf. The hafnium charge of +1.51e is significantly smaller than

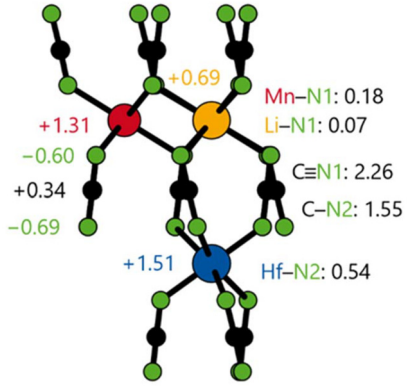

Fig. 4 Ionic and covalent bonding properties in $Li_2MnHf_2(NCN)_6$ by means of Löwdin atomic charges and integrated crystal orbital bond indices.

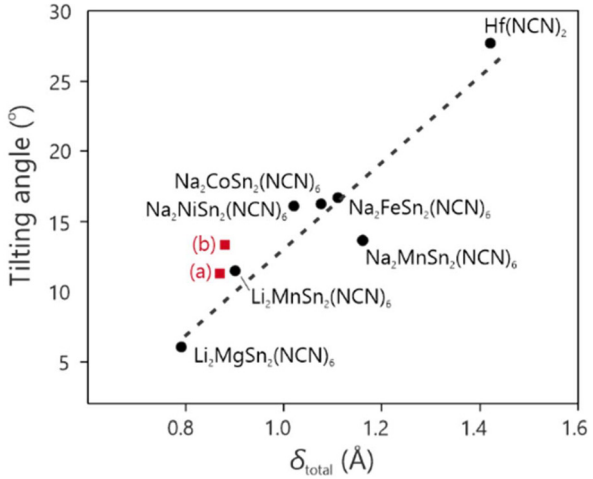

Fig. 5 Total distortion *versus* tilting angle encountered in all the reported quaternary compounds, $Hf(NCN)_2$, (a) $Li_2MnZr_2(NCN)_6$ and (b) $Li_2MnHf_2(NCN)_6$. The total distortion of the quaternaries was calculated with $\delta_{total} = (r_A - r_T) + r_M$, that of the binary $Hf(NCN)_2$ was calculated with $\delta_{total} = 2r_A$.[17,49]

+4*e*, rather surprising in the first place but explained by the energy-dependent COBI value showing significantly larger covalency for the Hf–N interaction than for the covalently almost negligible Mn–N and Li–N interactions, indicating a higher ionicity for the latter two. Indeed, the ICOBI (Hf–N) is equal to 0.54 for each of the six Hf–N distances, indicating a strongly covalent contribution. By contrast, ICOBI is only 0.18 and 0.07 for Mn–N and Li–N respectively. Such a behavior of the tetravalent metal atom was similarly observed for Ti^{4+} in Ti–O bonds in $BaTiO_3$.[42] Despite the difficulties normally encountered by DFT functionals in dealing with the cyanamide form of NCN, the orientation of single and triple bonds is mirrored by DFT calculations with bond orders of C–N1 = 2.26 and C–N2 = 1.55, in line with both the coordinative expectations and the experimental results.

The one-dimensionally extended NCN unit contrasts with the spherical oxide anion in its ability to tilt and bend, giving it a valuable advantage in terms of flexibility, allowing it to accommodate significant cation size differences. Our group recently developed an efficient method to describe these size differences within layers of NCN-containing compounds which can be expressed as a total distortion (δ_{total}).[49] In the present case of quaternary $A_2MT_2(NCN)_6$ compounds (*A*: an alkali metal, *M*: a divalent metal and *T*: a tetravalent metal) the total distortion is $\delta_{total} = (r_A - r_T) + r_M$. Given that a tilting of the NCN unit is a consequence of size differences, it is possible to establish a positive correlation between the tilting angle and the total distortion, δ_{total}. This can be clearly seen in Fig. 5 for quaternary compounds with composition $A_2MT_2(NCN)_6$ in which as the total distortion increases, the tilting angle of the NCN unit also increases in an approximately linear manner. In the two novel quaternary compounds, the NCN units are tilted away from the stacking axis with angles of 13.5(3)° and 11.5 (3)° for $Li_2MnHf_2(NCN)_6$ and $Li_2MnZr_2(NCN)_6$ respectively, consistent with the rest of the reported quaternary cyanamide compounds.

These tilt distortions in turn have an influence on the nitrogen positions, which affects the regularity of the metal octahedra. This can be expressed quantitatively by the quadratic elongation parameter (dimensionless λ_{oct}, equal to 1 for the ideal octahedron).[50] By setting this parameter against the total distortion δ_{total} individually on the three different metal sites of the quaternary compounds (Fig. 6), it appears that in the divalent metal site, Fig. 6(a), upon increasing total distortion, the octahedron tends rapidly towards a more regular one. A similar, albeit less pronounced, decreasing linear trend is also observed in the alkali metal site, Fig. 6(b). This tendency to rapidly approach the divalent site can be explained geometrically by the fact that the nitrogen atoms move along the distortion axis toward the divalent site. At the tetravalent metal site, however, the distortion appears to be independent from the total distortion as no trend is noticed. One explanation could also be of a steric nature, since hafnium shares space in its layer with a vacant site, the latter behaving like a huge cation augmenting the position of the nitrogen atoms, thus preventing the adoption of a regular octahedron and explaining why, as yet, only d^0 (Zr^{4+} and Hf^{4+}) or d^{10} (Sn^{4+}) cations have been realized at this position. Nonetheless, it is clear at the outset that a model based on geometrical criteria (such as ionic radii) is hardly justified for the tetravalent site (Hf) since the associated chemical bonding is largely covalent in nature, as shown before (Fig. 4).

As such, this analysis reveals a delicate balance between geometrical (size of the ions) and electronic (nature of the bond) requirements. By modifying these factors, one could target the synthesis, perhaps by SSM, of a whole host of other quaternary $A_2MT_2(NCN)_6$ compounds incorporating a complementary balance of metals over the three different sites.

The band structure of $Li_2MnHf_2(NCN)_6$ was calculated for the geometry-optimized crystal structure. The static calculation yields an indirect zero-temperature band gap of approximately

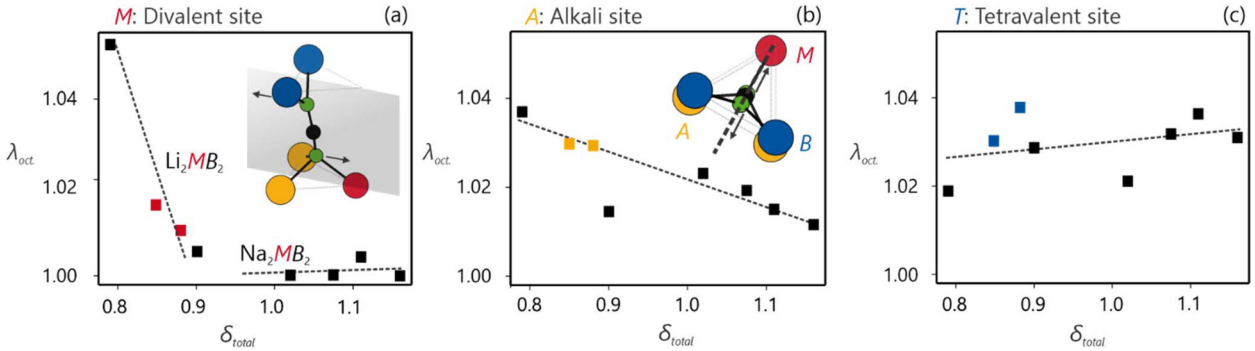

Fig. 6 Total distortion *vs.* quadratic elongation (calculated with $\lambda_{oct} = \sum_{i=1}^{6} \frac{(l_i/l_0)^2}{6}$) in quaternary cyanamides with a structure of $A_2MT_2(NCN)_6$ (a) divalent metal site (b) alkali metal site (c) tetravalent metal site.

2.4 eV similar to that calculated for $Na_2MnSn_2(NCN)_6$. In order to further investigate the electronic structure, density of states (DOS) and (fat) band structure calculations were analyzed. The total DOS is dominated by Mn 3d levels, Hf 5d levels and N 2p levels as was observed previously in other quaternaries.[22] Li, N 2s, and the remaining Mn levels show no significant contributions in the chosen energy range of −10 eV to +5 eV (Fig. 7).

The optical band gap was experimentally determined by UV–vis spectroscopy, yielding a value of 2.1 eV for the grey colored sample which is in very good accordance with the calculated data. Future work will look at varying the nature of the transition metal species at the '*M*' site in order to engender electronic band gaps and band edge positions suitable for solar energy harvesting (Fig. 8).

The magnetic susceptibility of $Li_2MnHf_2(NCN)_6$ was measured between 2–400 K in an applied field of 1000 Oe. Accounting for a 7.8 wt% of HfO_2 impurity suggested from Rietveld refinement, the data were corrected leading to the results shown in Fig. 9. These data exhibit paramagnetic behavior down to the lowest temperature measured with a progressive increase in χ_m with decreasing T and no signature for the onset of long-range magnetic order. At temperatures above 300 K Curie–Weiss behavior is observed, and a linear fit to the inverse susceptibility data (χ_m^{-1}) yields C = 3.89 cm^3 K mol^{-1}, which is a little smaller than that expected for a single non-

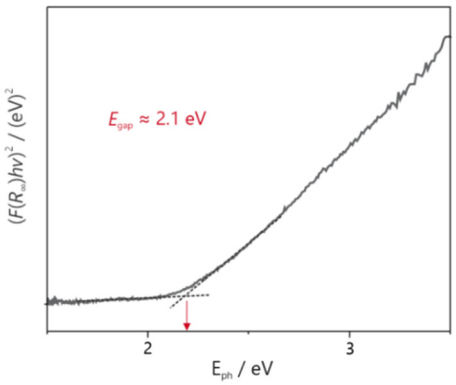

Fig. 8 Tauc plot of $Li_2MnHf_2(NCN)_6$ for indirect allowed transition (r = 1/2).

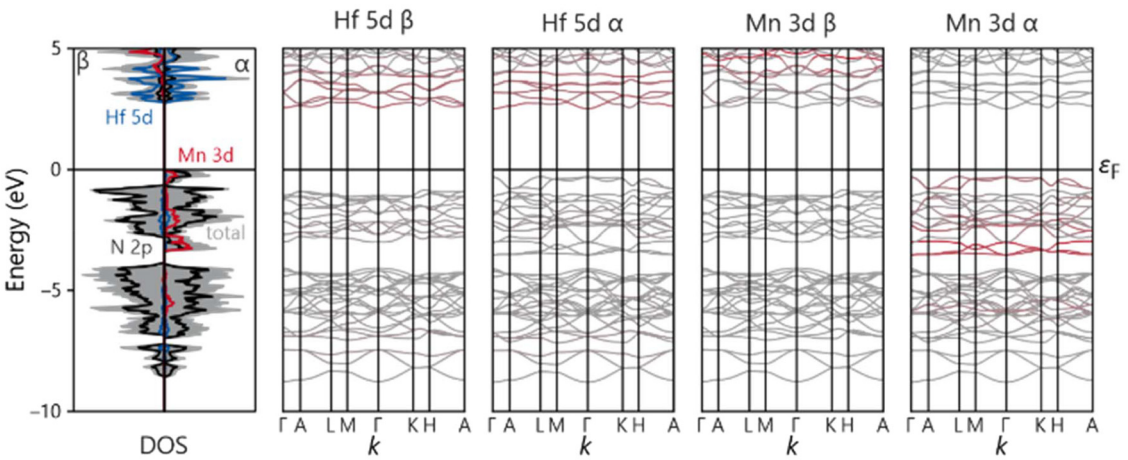

Fig. 7 Spin-polarized total DOS and contributing local DOS for $Li_2MnHf_2(NCN)_6$ (left). Calculated band structures with highlighted minority/majority spin channels of Mn 3d and Hf 5d (right).

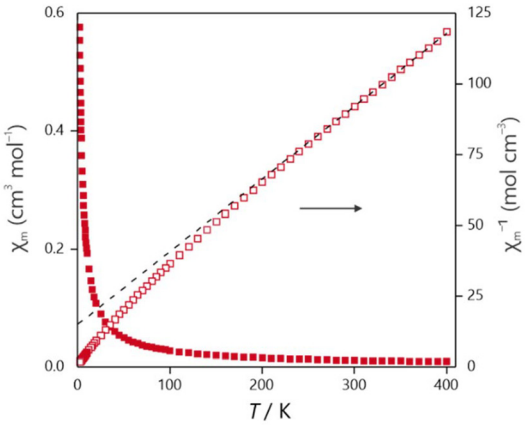

Fig. 9 Magnetic molar susceptibility (χ_m) *versus* temperature (T) plot for $Li_2MnHf_2(NCN)_6$ (left) measured at an applied field of H = 1000 Oe and inverse molar susceptibility (χ_m^{-1}) *versus* temperature (T) for $Li_2MnHf_2(NCN)_6$ (right).

interacting high-spin Mn^{2+} center (3.99–4.65 cm^3 K mol^{-1}),[51] and a negative Weiss temperature θ = −58.5 K indicative of predominantly antiferromagnetic interactions. This absence of a transition to a long-range magnetically order state is likely a result of the magnetic dilution of the octahedral metal positions, since in $Li_2MnHf_2(NCN)_6$ only 1/6 of the sites are occupied by paramagnetic cations. In contrast [NaCl]-derived MnNCN and [NiAs]-derived FeNCN, with fully occupied octahedral interstices, display Néel temperatures of 28 K and 350 K,[13,52] respectively, whilst $Cr_2(NCN)_3$ with 1/3 vacancies exhibits a transition to an ordered ferromagnetic state below 114 K.[53,54]

Conclusions

Herein we report the solid-state metathetic synthesis of two new quaternary cyanamides, $Li_2MnHf_2(NCN)_6$ and $Li_2MnZr_2(NCN)_6$. Both phases crystallize isostructurally to $Li_2MnSn_2(NCN)_6$ in a trigonal unit cell with $P\bar{3}1m$ symmetry, and both are stabilized by the extended nature of the NCN^{2-} anion which offers an additional flexibility, compared with O^{2-}, through the tilting of the cyanamide unit that is impossible in oxide chemistry. This helps to explain the absence of any comparable oxide analogues. The different coordination requirements of the metal cations result in an ordered design over the octahedral sites with corundum-like $[T_2(NCN)_3]^{2+}$ layers (T = Hf, Zr) alternating with $[Li_2Mn(NCN)_3]^{2-}$ layers. Meanwhile, a computational study using LOBSTER affords in-depth analysis of the bonding situation, revealing a higher degree of covalency in the Hf–N bonds, compared with more ionic Li–N and Mn–N bonds, which leads to the asymmetry of the NCN^{2-} moiety. In addition, a survey of all existing $A_2MT_2(NCN)_6$ quaternaries shows the capacity of the NCN unit to adapt to cation size differences through cooperative tilt distortions. Furthermore, analysis of the quadratic elongation of individual metal octahedra provides deeper insight into the subtle balance of geometric and electronic requirements of the constituent cations. The optical band gap was measured by UV-vis, giving a value of 2.1 eV, in very good agreement with the computed value. Magnetic susceptibility measurements suggest predominantly antiferromagnetic interactions (θ = −58.5 K), however, no signature for a transition to a long-range ordered state was observed, presumably resulting from the magnetic dilution of the octahedral metal sites, only 1/6 of which are occupied by paramagnetic Mn^{2+} cations. Future work will seek to vary the nature of the divalent transition metal species to engender band gaps suitable for photochemical applications and explore the electrochemical properties of this family.

Data availability

Crystallographic data for $Li_2MnHf_2(NCN)_6$ and $Li_2MnZr_2(NCN)_6$ have been deposited at the CCDC under 2382982 and 2382983,† respectively and can be obtained from **https://www.ccdc.cam.ac.uk/**.

Conflicts of interest

There are no conflicts to declare.

Acknowledgements

We thank Mr T. Storp for assistance with PXRD measurements and Dr Ing. Dr rer. nat. Jan van Leusen for the magnetic correction. AJC would also like to acknowledge the financial support of the Deutsche Forschungsgemeinschaft (Project number 441856704).

References

1 A. J. Corkett, O. Reckeweg, R. Pöttgen and R. Dronskowski, *Chem. Mater.*, 2024, **36**, 9107–9125.
2 M. T. Sougrati, A. Darwiche, X. Liu, A. Mahmoud, R. P. Hermann, S. Jouen, L. Monconduit, R. Dronskowski and L. Stievano, *Angew. Chem., Int. Ed.*, 2016, **55**, 5090–5095.
3 A. Eguia-Barrio, E. Castillo-Martinez, X. Liu, R. Dronskowski, M. Armand and T. Rojo, *J. Mater. Chem. A*, 2016, **4**, 1608–1611.
4 Q. Liu, Y. Liu, G. Dai, L. Tian, J. Xu, G. Zhao, N. Zhang and Y. Fang, *Appl. Surf. Sci.*, 2015, **357**, 745–749.
5 M. Kubus, R. Heinicke, M. Ströbele, D. Enseling, T. Jüstel and H.-J. Meyer, *Mater. Res. Bull.*, 2015, **62**, 37–41.
6 W. P. Clark and R. Niewa, *Z. Anorg. Allg. Chem.*, 2020, **646**, 114–119.
7 M. Krings, G. Montana, R. Dronskowski and C. Wickleder, *Chem. Mater.*, 2011, **23**, 1694–1699.

8 S. Yuan, Y. Yang, F. Chevire, F. Tessier, X. Zhang and G. Chenz, *J. Am. Ceram. Soc.*, 2010, **93**, 3052–3055.
9 H.-J. Meyer, *Dalton Trans.*, 2010, **39**, 5973–5982.
10 X. Liu, M. Krott, P. Müller, C. Hu, H. Lueken and R. Dronskowski, *Inorg. Chem.*, 2005, **44**, 3001–3003.
11 U. Berger and W. Schnick, *J. Alloys Compd.*, 1994, **206**, 0925–8388.
12 A. Frankand N. Caro, *Deutsches Reichspatent*, 88363, 1895.
13 G. Baldinozzi, B. Malinowska, M. Rakib and G. Durand, *J. Mater. Chem.*, 2002, **12**, 268–272.
14 X. Liu, L. Stork, M. Speldrich, H. Lueken and R. Dronskowski, *Chem. – Eur. J.*, 2009, **15**, 1558–1561.
15 M. Krott, X. Liu, B. P. T. Fokwa, M. Speldrich, H. Lueken and R. Dronskowski, *Inorg. Chem.*, 2007, **46**(6), 2204–2207.
16 M. Kubus, R. Heinicke, M. Ströbele, D. Enseling, T. Jüstel and H.-J. Meyer, *Mater. Res. Bull.*, 2015, **62**, 37–41.
17 L. Unverfehrt, M. Ströbele and H.-J. Meyer, *Z. Anorg. Allg. Chem.*, 2013, **639**, 22–24.
18 A. J. Corkett, K. Chen and R. Dronskowski, *Eur. J. Inorg. Chem.*, 2020, **27**, 2596–2602.
19 H. Bourakhouadar, J. Hempelmann, J. van Leusen, A. Drichel, L. Bayarjargal, A. Koldemir, M. K. Reimann, R. Pöttgen, A. Slabon, A. J. Corkett and R. Dronskowski, *J. Am. Chem. Soc.*, 2024, **146**, 26071–26080.
20 K. Dolabdjian, A. Kobald, C.-P. Romao and H.-J. Meyer, *Dalton Trans.*, 2018, **47**, 10249–10255.
21 A. J. Corkett and R. Dronskowski, *Dalton Trans.*, 2019, **48**, 15029–15035.
22 A. J. Corkett, Z. Chen, C. Ertural, A. Slabon and R. Dronskowski, *Inorg. Chem.*, 2022, **45**, 18221–18228.
23 X. Qiao, A. J. Corkett, R. P. Stoffel and R. Dronskowski, *Z. Anorg. Allg. Chem.*, 2021, **647**, 2162.
24 J. Glaser, H. Bettentrup, T. Jüstel and H.-J. Meyer, *Inorg. Chem.*, 2010, **49**(6), 2954–2959.
25 K. Dolabdjian, C. Castro and H.-J. Meyer, *Eur. J. Inorg. Chem.*, 2018, **44**, 1624–1630.
26 B. H. J. Toby, *Appl. Crystallogr.*, 2001, **34**, 210–213.
27 P. E. Blöchl, *Phys. Rev. B: Condens. Matter Mater. Phys.*, 1994, **50**, 17953.
28 G. Kresse and J. Hafner, *Phys. Rev. B: Condens. Matter Mater. Phys.*, 1993, **47**(1), 558–561.
29 G. Kresse and J. Furthmüller, *Comput. Mater. Sci.*, 1996, **6**(1), 15–50, 0927-0256.
30 G. Kresse and J. Furthmüller, *Phys. Rev. B: Condens. Matter Mater. Phys.*, 1996, **54**, 11169.
31 G. Kresse and D. Joubert, *Phys. Rev. B: Condens. Matter Mater. Phys.*, 1999, **59**, 1758.
32 J. P. Perdew, K. Burke and M. Ernzerhof, *Phys. Rev. Lett.*, 1996, **77**, 3865.
33 S. Grimme, S. Ehrlich and L. Goerigk, *J. Comput. Chem.*, 2011, **32**(7), 1456–1465.
34 H. J. Monkhorst and J. D. Pack, *Phys. Rev. B: Solid State*, 1976, **13**, 5188.
35 P. E. Blöchl, O. Jepsen and O. K. Andersen, *Phys. Rev. B: Condens. Matter Mater. Phys.*, 1994, **49**(23), 16223–16233.
36 S. L. Dudarev, G. A. Botton, S. Y. Savrasov, C. J. Humphreys and A. P. Sutton, *Phys. Rev. B: Condens. Matter Mater. Phys.*, 1998, **57**, 1505.
37 R. Nelson, P. M. Konze and R. Dronskowski, *J. Phys. Chem. A*, 2017, **121**, 7778–7786.
38 S. Maintz, V. L. Deringer, A. L. Tchougréeff and R. Dronskowski, *J. Comput. Chem.*, 2013, **34**(29), 2557–2567.
39 S. Maintz, V. L. Deringer, A. L. Tchougréeff and R. Dronskowski, *J. Comput. Chem.*, 2016, **37**(11), 1030–1035.
40 R. Nelson, C. Ertural, J. George, V. L. Deringer, G. Hautier and R. Dronskowski, *J. Comput. Chem.*, 2020, **41**(21), 1931–1940.
41 C. Ertural, S. Steinberg and R. Dronskowski, *RSC Adv.*, 2019, **9**(51), 29821–29830.
42 P. C. Müller, C. Ertural, J. Hempelmann and R. Dronskowski, *J. Phys. Chem. C*, 2021, **125**(14), 7959–7970.
43 K. B. Wiberg, *Tetrahedron Lett.*, 1968, **24**(3), 1083–1096.
44 I. Mayer, *Chem. Phys. Lett.*, 1983, **97**(3), 270–274.
45 I. Mayer, *J. Comput. Chem.*, 2007, **28**(1), 204–221.
46 R. D. Shannon, *Acta Crystallogr.*, 1976, **25**, 751–767.
47 H. J. Goldschmidt and M. J. Walker, *J. Appl. Crystallogr.*, 1969, **2**, 281.
48 R. Pöttgen, A. Corkett and R. Dronskowski, *Z. Kristallogr.*, 2023, **238**, 95–103.
49 J. Medina-Jurado, A. J. Corkett and R. Dronskowski, *Z. Kristallogr. – Cryst. Mater.*, 2024, **239**, 1–2.
50 K. Robinson, *Science*, 1971, **172**, 567–570.
51 H. Lueken, *Magnetochemie*, Teubner Verlag, Stuttgart, 1999.
52 M. Krott, A. Houben, P. Müller, W. Schweika and R. Dronskowski, *Phys. Rev. B: Condens. Matter Mater. Phys.*, 2009, **80**, 024117.
53 X. Tang, H. Xiang, X. Liu, M. Speldrich and R. Dronskowski, *Angew. Chem., Int. Ed.*, 2010, **49**, 4738–4742.
54 K. B. Sterri, C. Besson, A. Houben, P. Jacobs, M. Hoelzel and R. Dronskowski, *New J. Chem.*, 2016, **40**, 10512–10519.